Accepted Manuscript

Title: Ytterbium modification of pristine and molybdenum-modified hematite electrodes as a strategy for efficient water splitting photoanodes

Authors: Ainhoa Cots, Roberto Gómez

PII: S0926-3373(17)30716-6
DOI: http://dx.doi.org/doi:10.1016/j.apcatb.2017.07.067
Reference: APCATB 15899

To appear in: *Applied Catalysis B: Environmental*

Received date: 6-5-2017
Revised date: 17-7-2017
Accepted date: 24-7-2017

Please cite this article as: Ainhoa Cots, Roberto Gómez, Ytterbium modification of pristine and molybdenum-modified hematite electrodes as a strategy for efficient water splitting photoanodes, Applied Catalysis B, Environmentalhttp://dx.doi.org/10.1016/j.apcatb.2017.07.067

This is a PDF file of an unedited manuscript that has been accepted for publication. As a service to our customers we are providing this early version of the manuscript. The manuscript will undergo copyediting, typesetting, and review of the resulting proof before it is published in its final form. Please note that during the production process errors may be discovered which could affect the content, and all legal disclaimers that apply to the journal pertain.

ACCEPTED MANUSCRIPT

Ytterbium modification of pristine and molybdenum-modified hematite electrodes as a strategy for efficient water splitting photoanodes

Ainhoa Cots, Roberto Gómez*

Departament de Química Física i Institut Universitari d'Electroquímica, Universitat d'Alacant. Apartat 99, E-03080 Alacant, Spain

**Corresponding Author. Tel: +34 96 590 3748; email address: roberto.gomez@ua.es*

GRAPHICAL ABSTRACT

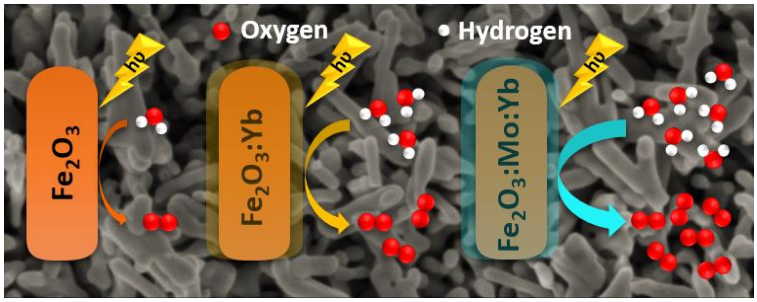

HIGHLIGHTS

- **YTTERBIUM MODIFICATION OF HEMATITE ELECTRODES CAN BE ACHIEVED BY IMPREGNATION.**
- **YTTERBIUM MODIFICATION LEADS TO PASSIVATION OF HEMATITE SURFACE STATES.**
- **HEMATITE ELECTRODE PHOTOCURRENT IS ENHANCED BY A FACTOR OF UP TO 13 UPON YTTERBIUM MODIFICATION.**
- **THERE IS SYNERGY BETWEEN MOLYBDENUM AND YTTERBIUM AS HEMATITE ELECTRODE MODIFIERS.**

Abstract

In recent years, the surface modification of photoanodes for photoelectrochemical water splitting with passivation overlayers has attracted considerable attention. In this respect, a novel, easy and simple methodology to introduce ytterbium oxide as an overlayer on hematite nanorod electrodes is reported in this work. The hematite electrodes were synthesized by means of a chemical bath method, while the ytterbium

ACCEPTED MANUSCRIPT

precursor was introduced through an impregnation method (drop-casting). FE-SEM, XRD, and XPS were employed to characterize the electrode both structurally and morphologically. The reported results reveal that the impregnation method did not cause apparent changes in the hematite structure and morphology, retaining the nanorod structure. Importantly, adding ytterbium yields a significant improvement in the photo-activity (14x at 0.23V vs Ag/AgCl) without altering significantly the photo-onset. The obtained results suggest that ytterbium induces the formation of a passivating layer, pointing to the fact that other lanthanide oxides would behave similarly. A study of a bifunctional modification of hematite employing ytterbium and molybdenum was also carried out. It reveals that the photocurrent obtained by employing both strategies increases with respect to that obtained with the application of only one of the procedures. Importantly, the order in which modification is done greatly affects the final electrode performance. Understandably, the best results are obtained when Mo is introduced prior to Yb, leading to a synergetic effect in the sense that the resulting photocurrent is larger than the sum of the photocurrents obtained through the application of one of the modifiers.

Keywords: *passivation; ytterbium; molybdenum; hematite; water splitting*

1. Introduction

Photoelectrochemical water splitting has attracted significant attention as a method for light to fuel conversion due to the fully renewable character of solar energy. Since the first demonstration of photoelectrochemical water splitting using TiO_2 [1–4], a large number of semiconductor materials have been studied as photoelectrodes such as WO_3 [5,6], GaP [7–9], α-Fe_2O_3 [10–14], $BiVO_4$ [15,16] and CuO [17,18]. These photoelectrodes have be used as either photoanodes or photocathodes depending on their chemical nature, electrochemical properties, and band structure.

ACCEPTED MANUSCRIPT

Among the different semiconductor materials, hematite (α-Fe_2O_3) keeps on being a promising candidate as a photoanode because of its stability, abundance, low cost, and favorable band gap [10,19,20]. However, its performance is limited because of the poor conductivity and extremely short hole diffusion length, which implies significant electron-hole recombination [9,10,21–23]. In recent years, several studies have focused on improving these limitations of hematite through different modification methodologies [24–28].

Several strategies have been employed in order to modify hematite among which the following stand: (i) the development of nanostructured architectures, (ii) the improvement of conductivity and promotion of charge transfer ability by metal ion doping, (iii) the reduction of the recombination rate through the employment of passivating layers and (iv) the improvement of the water oxidation kinetics using co-catalysts [10,29–33]. Surface modification of semiconductor photoelectrodes with passivating overlayers has recently attracted attention as an effective strategy to avoid trapping and hinder surface recombination. Different overlayers have been studied such as those of Ga_2O_3, Al_2O_3, TiO_2 and In_2O_3. In most cases, the onset potential for photoelectrochemical water oxidation on hematite was shifted to more negative values and the water oxidation photocurrent density was significantly increased [34–37].

One of the benefits of the overlayers described in the literature such as those of Al_2O_3, Ga_2O_3 or In_2O_3 is to facilitate unassisted water splitting tandem cells through an improvement of the photocurrent onset potential [34,38]. In the case of hematite photoanodes, the role of the overlayers has been extensively debated, suggesting that the main effect of these layers consists in the extension of the space charge region by surface state passivation rather than in surface catalysis [35,38–41].

The most frequently employed method for preparing a passivating overlayer is atomic layer deposition (ALD). However, in recent years, some studies have focused on simple water-based solution methods for the modification of hematite with overlayers,

ACCEPTED MANUSCRIPT

which are more cost-effective than ALD. In this way, Hisatomi *et al*. [34] reported the preparation of 13-group oxides (Al_2O_3, Ga_2O_3, In_2O_3) as overlayers through chemical bath deposition (CBD). In all these cases, the recombination centers of the photogenerated carriers were effectively blocked, which improved the PEC performance [3,34,42,43].

In this work, we present a novel procedure for surface passivation of hematite photoanodes with ytterbium(III)-rich oxygenated overlayers for efficient solar water splitting. The methodology employed to modify the hematite electrodes is that of impregnation (drop casting). The passivation of molybdenum doped hematite was also addressed and the beneficial effects of both passivation and doping were found to be compatible and even synergetic [44].

2. Experimental Section

2.1. Synthesis of (110) oriented hematite nanorods

The methodology employed to synthesize the (110) oriented hematite nanorods is based on the work of Vayssieres *et al.* [13], who proposed a synthetic route to control the growth from aqueous solution. The synthesis is based on a chemical bath deposition procedure followed by a thermal treatment [11–13]. All solutions were prepared with deionized water with a resistivity higher than 15 $M\Omega \cdot cm^{-1}$. The experimental procedure consists of adding 100 ml of an aqueous solution containing 0.15 $mol \cdot l^{-1}$ ferric chloride ($FeCl_3 \cdot 6H_2O$, Sigma-Aldrich, 99%) and 1 $mol \cdot l^{-1}$ sodium nitrate ($NaNO_3$, Panreac, 99%) into a regular stopped flask containing fluorine tin oxide (FTO) glass substrates almost vertically supported on the flask wall. Subsequently, the flask is heated in a regular stove at 100^0C for 6h. Finally, a heat treatment in air at 600^0C for at least 1 h is required to obtain the thermodynamically stable crystallographic phase of ferric oxide (hematite), with a nanorod-based morphology.

ACCEPTED MANUSCRIPT

2.1.1. Modification by Yb addition through drop-casting

Once the hematite nanorod thin films were prepared, the Yb-precursor was added through an impregnation method (drop casting). The employed precursor was ytterbium chloride hexahydrate ($YbCl_3 \cdot 6H_2O$, Sigma-Aldrich, 99.9%). By varying the concentration of the ytterbium precursor solution from 0.072 to 1.44 mM, different quantities of Yb were deposited. The precursor concentrations corresponding to the nomenclature employed together with the resulting nmol of $Yb \cdot cm^{-2}$ values are detailed in Table 1. Immediately after applying the drop casting procedure, the electrodes were dried overnight at 100^0C, followed by a heat treatment at 450^0C for 30 min.

2.1.2. Modification by the incorporation of Yb and Mo

A bifunctional modification was carried out. A molybdenum precursor was added by drop casting to the Yb-modified hematite (H_Yb_Mo samples) or alternatively the Yb modification described above was applied to the Mo-modified hematite (H_Mo_Yb samples). The Mo employed precursor was ammonium heptamolybdate tetrahydrate ($(NH_4)_6Mo_7O_{24} \cdot 4H_2O$, Fluka, 99%) with a concentration of 0.182 mM, corresponding to 6.8 nmol of $Mo \cdot cm^{-2}$ [44].

2.2. Sample characterization

The morphology of the different samples was studied by FE-SEM micrographs (Field Emission Scanning Electron Microscopy), (Zeis Merlin VP Compact). The microscope employed is equipped with an energy dispersive X-ray spectrometer (EDS), (Bruker Quantax 400).

The crystal structure of hematite was identified by X-ray Diffraction (Bruker D8-Advance, using Cu Ka radiation) with the rotatory anode operating at 40 kV and 40 mA in the 2Θ range from 20^0 to 70^0 using $1^0 \cdot min^{-1}$ as a step scan.

ACCEPTED MANUSCRIPT

X-ray Photoelectron Spectroscopy (XPS) was used for compositional analysis and for characterizing the iron, ytterbium, and molybdenum oxidation states (K-Alpha Thermo-Scientific).

2.3. (Photo)electrochemical characterization

A standard three-electrode cell was employed to carry out the (photo)electrochemical measurements, using the hematite film (pristine, modified with ytterbium or modified with both ytterbium and molybdenum) as the working electrode (1.2 cm^2 area) and an $Ag/AgCl/KCl_{sat}$ as a reference electrode (to which all the potentials are referred). The counter electrode used was a platinum wire. The working electrolyte solution was a N_2-purged 1 $mol \cdot l^{-1}$ NaOH (Panreac, 98%). A scanning potentiostat (Potentiostat/Galvanostat AUTOLAB PGSTAT30) was used to record voltammograms in the dark and under illumination at a scan rate of 50 $mV \cdot s^{-1}$ in the case of cyclic voltammetry or 10 $mV \cdot s^{-1}$ in the case of linear sweep voltammetry. Mott-Schottky plots and Electrochemical Impedance Spectra (range from 10 kHz to 0.1 Hz) were also measured with this piece of equipment. The lamp used for illumination was a 1000 W ozone-free xenon arc lamp (ORIEL Newport 66921 Lamp power 450-1000 W). The lamp radiation was passed through a water filter and a radiation cut off filter (Newport FSR-KG3 $\lambda \geq 350$ nm). The light intensity was measured with a thermopile (Thorlabs PM100D) with an incident power density of around 250 $mW \cdot cm^{-2}$. Illumination was also performed with a solar simulator (Abett, 550W) at 1sun (AM 1.5G).

3. Results and discussion

3.1. Sample characterization

The FE-SEM images of α-Fe_2O_3 nanorods in the presence and in the absence of ytterbium are shown in Fig. 1. An oriented 3D array of nanorods is observed as expected from the application of a method based on the work of Vayssieres *et al.* [11–13]. As observed in Fig. 1b, the addition of 4.8 nmol $Yb \cdot cm^{-2}$ (H_Yb2) does not cause

ACCEPTED MANUSCRIPT

noticeable changes in the obtained nanorods. The thickness of the films, deduced from cross-sectional images (Fig. 1c-d), is of about 400nm regardless of the presence of Yb. The FE-SEM images of hematite modified with both ytterbium and molybdenum are not shown because again, no changes are discernible.

The X-ray diffractogram of pristine hematite reveals the formation of predominantly (110) oriented hematite (α-Fe_2O_3) as shown in Fig. S1 (supplementary material). The addition of ytterbium and molybdenum does not affect the formation of the (110)-oriented hematite nanorods.

XPS spectra for different hematite samples are shown in Fig. 2. As observed, the XPS spectra of Fe 2p (Fig. 2a) are quite similar in all cases and attributed completely to Fe^{3+}. Fig. 2b shows the Yb 4d XPS spectra for the electrodes H_Yb2, H_Yb2_Mo and H_Mo_Yb2. Those for the former samples are similar and the characteristic peaks of Yb $4d_{5/2}$ and $4d_{3/2}$ are centered at 185.2 eV and 192.9 eV, respectively, suggesting that Yb^{3+} is present in both samples in an environment similar to that of ytterbium oxide. However, in the case of the H_Mo_Yb2 sample, there is a clear shift of the $4d_{5/2}$ peak toward higher binding energies (186 eV), which attests that there exists a significant interaction with Mo species [45,46]. Finally, the Mo 3d XPS spectra are shown in Fig. 2c. Comparing the spectra in the presence (red) and in the absence (green) of ytterbium in the sample, it is clear that the oxidation state of molybdenum is not the same. In the absence of ytterbium, the Mo $3d_{5/2}$ peak is centered at 232.5 eV, while in its presence, the Mo XPS peaks shift to lower values of binding energy. According to the data published by Anwar *et al.*, our results reveal that in absence of ytterbium its oxidation state is +6, while in its presence, the resulting Mo oxidation state is +5 [47–49].

3.2. (Photo)electrochemical characterization

3.2.1. Behavior in the dark

ACCEPTED MANUSCRIPT

Fig. 3 shows cyclic voltammograms obtained in the dark for a pristine hematite electrode (black) and a hematite electrode modified with 4.8 nmol Yb·cm^{-2} (H_Yb2) (red). Focusing on the black curve, a capacitive current is observed at potentials below -0.2V, which can be attributed to an accumulation region linked to either conduction band or surface states. At potentials positive to 0.4V, there is a region linked to a pseudocapacitive contributions associated with the oxidation of surface Fe (III) to Fe (IV) and vice versa, together with a faradaic current due to the generation of oxygen. Upon the addition of 4.8 nmol Yb·cm^{-2} (H_Yb2) (red), the accumulation region virtually disappears, this observation clearly indicating that the accumulation region is linked to surface states that become blocked upon Yb modification. At potentials positive to 0.4V, the region linked to the Fe(IV)/Fe(III) surface redox couple also decreases due to the effective surface blockage mentioned above.

The modification was tried for different molar concentrations of the ytterbium precursor ranging from 0.072 to 1.440 mM (2.4 to 48 nmol Yb·cm^{-2}). In all cases, the accumulation region and the region linked to the surface Fe(IV)/Fe(III) redox couple dramatically diminishes (Fig. S2).

3.2.2. Behavior under illumination

Fig. 4a shows linear voltammograms for pristine hematite electrodes and samples with different Yb loadings under illumination (250 mW·cm^{-2}, λ>350nm) in aqueous N_2-purged 1M NaOH. Before the addition of ytterbium, the pristine hematite electrode describes the typical response of nanorod samples, a photo-onset at around -0.53V in 1M NaOH and a low photocurrent of 0.01 mA·cm^{-2} at 0.23V. After the addition of 4.8 nmol Yb·cm^{-2} (H_Yb2), the onset of the photocurrent slightly shifts to -0.53V while the shape of the photocurrent vs. potential curve remains virtually unaltered. However, the current density increases rapidly attaining 0.13 mA·cm^{-2} at 0.23V, and showing a plateau at around 0.3 mA·cm^{-2} from 0.3 to 0.4V. The same experiment was carried out with different loadings of Yb, yielding the same qualitative behavior. The inset in Fig. 4

ACCEPTED MANUSCRIPT

shows the photocurrent density obtained at 0.23V for the different electrodes studied. The optimum photoresponse is obtained for 4.8 nmol Yb·cm^{-2} (H_Yb2). It is worth noting that the addition of more than 7.2 nmol Yb·cm^{-2} (H_Yb3) or less than 4.8 nmol Yb·cm^{-2} (H_Yb2) does not trigger a significant improvement in the behavior of the hematite electrodes.

Fig. 5 shows a comparison of a linear voltammograms obtained under illumination (250 mW·cm^{-2}, λ>350nm) for a pristine hematite electrode and the optimum Yb-modified electrode (H_Yb2). The experiments were carried out with both electrode-electrolyte (*EE*, Fig. 5a) and semiconductor-electrolyte (*SE*, Fig. 5b) illumination in order to simulate the behavior of a photoanode in a prospective tandem cell. The inset in Fig.5a shows photocurrent transients under the same illumination conditions and recorded at 0.23 V vs. Ag/AgCl. Fig. 5b shows that the presence of ytterbium increases the photocurrent obtained under SE illumination to a lesser relative extent than under EE illumination.

3.2.3. Results obtained with the addition of Yb and Mo

In the following we focus on the sequential co-modification with i) Mo first and then Yb and ii) Yb first and then Mo. Fig. 6 shows a series of voltammograms measured in N_2-purged 1M NaOH in the dark (Fig. 6a) and under both EE (Fig. 6b) and SE (Fig. 6c) illumination (250 mW·cm^{-2}, λ>350nm). The responses of electrodes made of pristine hematite and hematite electrodes modified with different loadings of Yb are included. As unveiled in a recent study from our laboratory, the addition of molybdenum increases the accumulation region likely due to an increment in the conductivity of the film [44]. An intermediate situation is now found for samples modified with both 4.8 nmol Yb·cm^{-2} and 6.8 nmol of Mo·cm^{-2} (H_Yb2_Mo and H_Mo_Yb2). Importantly, for these electrodes, particularly for the latter, the pseudocapacitive region at high potentials (associated with the Fe (IV)/Fe (III) surface redox couple) is suppressed. This is also reflected in the constancy of the flat band potential upon illumination (see

ACCEPTED MANUSCRIPT

Table S1). Under EE illumination (Fig. 6b) all the modified electrodes exhibit an increment in the photocurrent compared to pristine hematite electrode, obtaining a maximum for the electrode modified with 6.8 nmol Mo·cm^{-2} followed by 4.8 nmol Yb·cm^{-2} (H_Mo_Yb2), which demonstrates that a bifunctional modification is correctly achieved in terms of photocurrent. Interestingly, the photocurrents obtained in this case are significantly larger than the sum of the photocurrents obtained after applying one of the modifiers (either Mo or Yb). In this case, apart from the increment in the photocurrent, the photo-onset shifts to more positive potentials, up to a value of around -0.34V. Focusing on SE illumination (Fig. 6c), hematite modified with 4.8 nmol Yb·cm^{-2} (H_Yb2) shows the lowest photocurrent enhancement, which could be due to an inhomogeneous distribution of ytterbium throughout the film, as described above. As in the case of EE illumination, the simultaneous presence of molybdenum and ytterbium (H_Yb2_Mo, H_Mo_Yb2) leads to the maximum enhancement, particularly for H_Mo_Yb2 electrode, illustrating anew the additive and even synergetic effect of both modifiers. Additional measurements were carried out under 1 sun SE illumination (see Fig. S3 in Supplementary data) for the optimum electrodes. The results obtained with the solar simulator are in qualitative agreement to those obtained with the ozone-free xenon arc lamp.

Experiments with the addition of an efficient hole scavenger (0.5 M H_2O_2) were also carried out with comparative purposes as it is assumed that, in such a case, all the photogenerated holes that arrive at the electrode/electrolyte interface are collected. In principle, these experiments allow for distinguishing between bulk and surface recombination processes involved in the photoelectrochemical oxidation of water [51]. These measurements are shown in Fig. S4 (Supplementary data) and were performed under 1 sun SE illumination at 0.23V vs. Ag/AgCl for pristine hematite, hematite modified with either 4.8 nmol Yb·cm^{-2} (H_Yb2) or 6.8 nmol of Mo·cm^{-2} first and 4.8

ACCEPTED MANUSCRIPT

nmol Yb·cm^{-2} second (H_Mo_Yb2) both in the absence and in the presence of 0.5M H_2O_2.

3.2.4. Mott-Schottky and Electrochemical Impedance Spectroscopy analysis.

In order to determine the flat band potential and the carrier density for the different electrodes, Mott-Schottky analysis was performed at a frequency of 1 kHz. It should be borne in mind that the employed electrodes have a 3D morphology, in the sense that the real interfacial area is significantly larger than the geometric one. As long as the dimension of the nanoobjects (diameter of nanorods in this case) is larger than that of the space charge region, the Mott-Schottky equation should take into account the real surface area rather than the geometric one by considering the electrode roughness. If we take into account that the roughness factor (*r*) can be expressed as:

$$r = \frac{A_{real}}{A_{geom}} \qquad (1)$$

Where A_{real} and A_{geom} correspond to the real and geometric (project) electrode surface are. The Mott-Schottky equation can be rewritten as [44]:

$$\frac{A_{geom}^2}{C_{sc}^2} = \frac{2}{e\varepsilon\varepsilon_0 N_d r^2}\left(E - E_{fb} - \frac{kT}{e}\right) \qquad (2)$$

where C_{SC} is the capacitance of the space charge region, ε_{sc} is the dielectric constant of the semiconductor, ε_0 is the permittivity of free space, N_d is the donor density (electron donor concentration for an *n*-type semiconductor), r is the roughness factor, E is the applied potential and E_{fb} is the flat band potential.

Unfortunately, the use of Eq. (2) is not widespread. A more detailed discussion on the use of the Mott-Schottky equation for nanostructured electrodes is underway and will be published elsewhere. In the case of a nanorod electrode, the roughness factor can be determined as:

ACCEPTED MANUSCRIPT

$$r = 1 + 2\pi RhN_{col} \quad (3)$$

where R is the average nanorod radius, h is the average nanorod height and N_{col} is the average density of nanorods per cm^2. For the present electrodes, the roughness factor attains a value of 10.6 [44].

Fig. 7 shows Mott-Schottky plots obtained in the dark for pristine hematite and hematite modified with 4.8 nmol Yb·cm^{-2} (H_Yb2) electrodes. In the inset table, the flat band potential and the carrier density obtained from Mott-Schottky plots are gathered. To obtain the carrier density, a value of ε_{sc}=25 was used [50]. The flat band potential obtained in the case of hematite modified with 4.8 nmol Yb·cm^{-2} (H_Yb2) is similar to that of pristine hematite, with a minor shift of 10 mV to positive potentials. In the presence of ytterbium, the carrier density increases, enhancing the n-type character of the oxide.

The same analysis was carried out under EE illumination (250 mW·cm^{-2}, λ>350nm) (Fig. S5, supplementary material), and the flat band potential was not found to change significantly although the carrier density increases in both cases with respect to the dark measurements, being larger again for hematite modified with 4.8 nmol Yb·cm^{-2} (H_Yb2).

Regarding the electrodes modified with both ytterbium and molybdenum, Fig. S6 shows the Mott-Schottky plots obtained (a) in the dark and (b) under EE illumination (250 mW·cm^{-2}, λ>350nm) for pristine hematite, H_Mo, H_Yb2_Mo and H_Mo_Yb2 electrodes. The resulting flat band potentials obtained in the case of hematite modified with 4.8 nmol Yb·cm^{-2} and 6.8 nmol of Mo·cm^{-2} (H_Yb2_Mo) slightly shift to less negative potentials with respect to pristine hematite. Interestingly, the H_Yb2_Mo electrode has a value of N_d higher than in the case of the sole addition of Yb but lower than when only Mo is added. In the case of H_Mo_Yb2 electrode there is a significant shift of the flat band potential toward less negative values together with a doping

ACCEPTED MANUSCRIPT

density similar to that of pristine hematite. In table S2, the flat band potential and the carrier density obtained from Mott-Schottky plots are gathered.

Electrochemical impedance spectroscopy (EIS) experiments were done under illumination (250 $mW \cdot cm^{-2}$, λ>350nm) for pristine hematite, H_Yb2 and H_Mo_Yb2 in order to study the kinetics of charge transfer processes under PEC operating conditions. Two potentials were chosen: -0.30 V (close to the photo-onset potential) and 0.23 V (O_2/OH^- equilibrium potential). The charge transfer resistance at the semiconductor/electrolyte interface is associated to the radius of the semicircle in the frequency range 1-100Hz [52]. As shown in Fig. 8, Nyquist plots collected at either -0.30 V or 0.23 V for the optimum electrodes, show that the electrode modified with molybdenum first and ytterbium has a much smaller impedance arc radius at both potentials, indicating that the charge transfer kinetics is much faster.

4. Discussion

The modification of hematite with Yb seems to passivate the hematite surface states below the conducting band edge. This role is highlighted by the changes that occur in the electrochemical response of the modified electrodes in the dark. In fact, the region of charge accumulation at negative potentials virtually disappears indicating that the surface states become blocked upon Yb-modification. At positive potentials, the region linked to the Fe(IV)/Fe(III) surface redox couple also decreases due to a partial blockage of surface states associated with the valence band edge. Moreover, under EE illumination the photo-onset is virtually unaltered while the photocurrent density increases rapidly, obtaining an optimum response for 4.8 nmol $Yb \cdot cm^{-2}$ (H_Yb2). Under SE illumination, there is also a photocurrent increase, but smaller in relative terms than that observed for EE illumination. In the case of SE illumination, the behavior of pristine hematite is superior to that of EE illumination. This is probably linked to the relatively low effective diffusion coefficient of photo-generated electrons and the fast recombination of electrons with holes trapped in surface states. Under SE illumination,

ACCEPTED MANUSCRIPT

the carriers are generated closer to the contact, which facilitates the arrival of electrons to the conducting substrate. In any case, this makes that the relative improvement of the photo-response tends to be smaller than for EE illumination. There could be a second reason explaining the different enhancements for EE and SE illumination linked to a possible non-homogeneous distribution of Yb, which would concentrate on the outer part of the nanostructured film (in agreement with XPS results) where most carriers are generated under EE illumination. On the other hand, the shape of the photocurrent transients at 0.23 V vs Ag/AgCl significantly changes upon the introduction of Yb, indicating that modification diminishes the tendency of holes to be surface trapped and therefore recombination. Interestingly, the determination of charge collection and charge injection efficiencies (see table S2 in the Supplementary data) reveals that modification with Yb dramatically increases charge injection efficiency (by a factor of 4) while the change in the charge collection efficiency is less important. This observation further highlights the profound modification that Yb causes in the charge dynamics in the surface, not being so important its change in the hematite bulk. In agreement with these results, EIS measurements indicates a diminution the the charge transfer resistance upon modification with Yb.

Another piece of evidence on the Yb effect comes from Mott-Schottky plots, whose analysis (see Table S3 in the Supplementary data) confirms that the ytterbium overlayer leaves the flat band potential unchanged as expected for the case of surface passivation, while an increase in the majority carrier density is also deduced from the sloped of the plots. These results are in agreement with those reported for hematite passivation with Al_2O_3 by Le Formal *et al.* [35]. In fact, detailed studies with X-Ray spectroscopy techniques have revealed that the heterostructures constituted by either TiO_2 [53] or Al_2O_3 [54] lead to an electron enrichment of the hematite phase. A similar mechanism could be involved for oxygenated ytterbium surface species.

ACCEPTED MANUSCRIPT

Interestingly co-modification with Yb and Mo shows that their effects are close to additive when Yb is applied first, while there is a clear synergy when Mo is applied first as deduced from a photoresponse larger than the sum of that resulting upon the application of one of the modifiers. Apart from the practical importance of this finding, it suggests a distinct distribution of both modifiers throughout the film and possibly a different mechanism of action.

As explained above, Yb species would mainly passivate surface states leading to an increase in the majority carrier mobility together with a certain degree of electron enrichment. This role would not be significantly affected by the presence of Mo, although slight changes in the Yb 4d XPS peaks are obvious when Yb is applied to a sample previously modified with Mo. This together with the fact that for the H_Mo_Yb2 electrode the Fe(IV)/Fe(III) surface redox couple is fully suppressed indicate that the co-modification leads to a very effective passivation of the surface states appearing above the valence band edge. These surface states would be directly linked to hole trapping and thus to an increased recombination. In fact, charge collection and charge injection efficiencies for the latter sample in comparison with the H_Yb2 sample show that co-modification leads to charge injection efficiencies that are almost twice those observed for the sample modified only with Yb. Accordingly a further decrease in the charge transfer resistance is deduced from the EIS experiments. It is also worth noting that in the presence of Yb, Mo is present in the +5 oxidation state (instead of the +6 value found in the case of samples modified only with Mo). This indicates that the Mo role as a dopant increasing the n-character of hematite is inhibited, which is compatible with the fact that all the Yb-containing samples have the same value of N_d irrespective of the presence of Mo.

5. Conclusions

In summary, hematite nanorod photoanodes were properly passivated by the modification with ytterbium-based overlayers by employing a novel, simple and easy

ACCEPTED MANUSCRIPT

impregnation method (drop-casting). In the presence of ytterbium in the dark, the capacitive currents observed at lower potentials virtually disappear, which indicates that they should be linked to surface states. This suggests that Yb oxygenated species effectively block surface Fe, which also explains the blockage of the pseudocapacitive process appearing at high potentials associated to the Fe(IV)/Fe(III) surface redox couple. The modification of the nanostructured hematite photoanodes with 4.8 nmol of $Yb \cdot cm^{-2}$ (H_Yb2) shows a 14-fold improvement in the photo-response with respect to pristine hematite, the photocurrent onset remaining virtually unaltered. Upon the addition of ytterbium, no changes in the morphology of the film were observed. The XPS spectra suggests that the ytterbium is in a chemical form close to that of Yb_2O_3, which points to the fact that Yb_2O_3 would passivate surface states, avoiding trapping of conduction band electrons and diminishing their effective mass. In addition, an electron enrichment would take place as revealed by a Mott-Schottky analysis.

A bifunctional modification with Mo and Yb is correctly achieved, showing a synergetic character. Importantly, the order in which the modifiers are incorporated has a clear effect on the performance of the resulting electrodes, being preferable the modification with Mo first and then with Yb because the last one would have the role of forming a passivation layer at the electrode surface together with leading to a certain degree of electron enrichment.

In addition, this study demonstrates its bifunctionalization with ytterbium and molybdenum is possible and that the effects of these modifiers are synergetic if Mo is introduced first. Admittedly, with the bifunctionalization of hematite with ytterbium and molybdenum the photocurrent onset shifts to less negative potentials. Future studies should focus on solving this limitation by employing others elements to bifunctionalize hematite electrodes. Studies along these lines are underway in our laboratory.

ACCEPTED MANUSCRIPT

Associated content

Supplementary data associated with this article can be found, in the online version, at http://dx.doi.org/10.1016/j.apcatb.2017.XX.XXX. *Supplementary Materials: X-ray diffractograms, Cyclic voltammograms in the dark for ytterbium-modified hematite electrodes, Linear scan voltammograms under standardized illumination, Transient photocurrent experiments in the presence/absence of a hole scavenger: charge separation and injection efficiencies and additional Mott-Schottky plots.*

Acknowledgements

Authors are grateful to MINECO of Spain for the financial support MAT2015-71727-R (FONDOS FEDER). A.C. wants to acknowledge the University of Alicante for a predoctoral grant (FPU-UA).

ACCEPTED MANUSCRIPT

References

[1] A. Fujishima, K. Honda, Electrochemical photolysis of water at a semiconductor electrode, Nature. 238 (1972) 37–38.

[2] T. Berger, D. Monllor-Satoca, M. Jankulovska, T. Lana-Villarreal, R. Gómez, The electrochemistry of nanostructured titanium dioxide electrodes, ChemPhysChem. 13 (2012) 2824–2875.

[3] G.K. Larsen, B.C. Fitzmorris, C. Longo, J.Z. Zhang, Y. Zhao, Nanostructured homogenous CdSe–TiO_2 composite visible light photoanodes fabricated by oblique angle codeposition, J. Mater. Chem. 22 (2012) 14205.

[4] F. Xu, J. Mei, M. Zheng, D. Bai, D. Wu, Z. Gao, et al., Au nanoparticles modified branched TiO_2 nanorod array arranged with ultrathin nanorods for enhanced photoelectrochemical water splitting, J. Alloys Compd. 693 (2017) 1124–1132.

[5] C. Fàbrega, S. Murcia-López, D. Monllor-Satoca, J.D. Prades, M.D. Hernández-Alonso, G. Penelas, et al., Efficient WO_3 photoanodes fabricated by pulsed laser deposition for photoelectrochemical water splitting with high faradaic efficiency, Appl. Catal. B Environ. 189 (2016) 133–140.

[6] S.L. Liew, Z. Zhang, T.W.G. Goh, G.S. Subramanian, H.L.D. Seng, T.S.A. Hor, et al., Yb-doped WO_3 photocatalysts for water oxidation with visible light, Int. J. Hydrogen Energy. 39 (2014) 4291–4298

[7] C. Liu, J. Sun, J. Tang, P. Yang, Zn-doped p-type gallium phosphide nanowire photocathodes from a surfactant-free solution synthesis., Nano Lett. 12 (2012) 5407–5411.

[8] J. Sun, C. Liu, P. Yang, Surfactant-free, large-scale, solution-liquid-solid growth of gallium phosphide nanowires and their use for visible-light-driven hydrogen production from water reduction., J. Am. Chem. Soc. 133 (2011) 19306–19309.

[9] G. Wang, Y. Ling, H. Wang, L. Xihong, Y. Li, Chemically modified nanostructures for photoelectrochemical water splitting, J. Photochem. Photobiol. C Photochem. Rev. 18 (2014) 35–51.

[10] K. Sivula, F. Le Formal, M. Grätzel, Solar water splitting: Progress using hematite (α-Fe_2O_3) photoelectrodes, ChemSusChem. 4 (2011) 432–449.

[11] T. Lindgren, H. Wang, N. Beermann, L. Vayssieres, A. Hagfeldt, S.-E. Lindquist, Aqueous photoelectrochemistry of hematite nanorod array, Sol. Energy Mater. Sol. Cells. 71 (2002) 231–243.

[12] N. Beermann, L. Vayssieres, S.-E. Lindquist, A. Hagfeldt, Photoelectrochemical Studies of Oriented Nanorod Thin Films of Hematite, J. Electrochem. Soc. 147 (2000) 2456–2461.

[13] L. Vayssieres, N. Beermann, S.E. Lindquist, a. Hagfeldt, Controlled aqueous chemical growth of oriented three-dimensional crystalline nanorod arrays: Application to iron(III) oxides, Chem. Mater. 13 (2001) 233–235.

[14] Q. Li, J. Bian, N. Zhang, D.H.L. Ng, Loading $Ni(OH)_2$ on the Ti-doped hematite photoanode for photoelectrochemical water splitting, Electrochim. Acta 155 (2015) 383–390.

ACCEPTED MANUSCRIPT

[15] P. Bornoz, F.F. Abdi, S.D. Tilley, B. Dam, R. Van De Krol, M. Grätzel, et al., A bismuth vanadate-cuprous oxide tandem cell for overall solar water splitting, J. Phys. Chem. C. 118 (2014) 16959–16966.

[16] J. Quiñonero, T. Lana-Villarreal, R. Gómez, Improving the photoactivity of bismuth vanadate thin film photoanodes through doping and surface modification strategies, Appl. Catal. B Environ. 194 (2016) 141–149.

[17] H. Oh, H. Ryu, W. Lee, Effects of copper precursor concentration on the growth of cupric oxide nanorods for photoelectrode using a modified chemical bath deposition method, J. Alloys Compd. 620 (2015) 55–59.

[18] Y. Hsu, C. Yu, H. Lin, Y. Chen, Y. Lin, Template synthesis of copper oxide nanowires for photoelectrochemical hydrogen generation, J. Electroanal. Chem. 704 (2013) 19–23.

[19] G. Gurudayal, S.Y. Chiam, M.H. Kumar, P.S. Bassi, H.L. Seng, J. Barber, et al., Improving the efficiency of hematite nanorods for photoelectrochemical water splitting by doping with manganese, ACS Appl. Mater. Interfaces. 6 (2014) 5852–5859.

[20] J.J. Deng, A.W. Pu, M. Li, J. Gao, H. Zhang, J. Zhong, et al., Hematite nanostructures for high efficient solar water splitting, Int. Conf. Nanotechnol., (2014) 75–78.

[21] N. Iordanova, M. Dupuis, K.M. Rosso, Charge transport in metal oxides: a theoretical study of hematite α-Fe_2O_3, J. Chem. Phys. 122 (2005) 144305–144310.

[22] T. Nakau, Electrical conductivity of α-Fe_2O_3, J. Phys. Soc. Japan. 15 (1960) 727.

[23] N.J. Cherepy, D.B. Liston, J.A. Lovejoy, H. Deng, J.Z. Zhang, Ultrafast studies of photoexcited electron dynamics in γ- and α-Fe_2O_3 semiconductor nanoparticles, J. Phys. Chem. B. 102 (1998) 770–776.

[24] O. Zandi, A.R. Schon, H. Hajibabaei, T.W. Hamann, Enhanced Charge Separation and Collection in High-Performance Electrodeposited Hematite Films, Chem. Mater. 28 (2016) 765–771.

[25] F. Malara, A. Minguzzi, M. Marelli, S. Morandi, R. Psaro, V. Dal Santo, et al., α-Fe_2O_3 /NiOOH: An Effective Heterostructure for Photoelectrochemical Water Oxidation, ACS Catal. 5 (2015) 5292–5300.

[26] H. Bemana, S. Rashid-Nadimi, Effect of sulfur doping on photoelectrochemical performance of hematite, Electrochim. Acta. 229 (2017) 396–403.

[27] J.-W. Jang, C. Du, Y. Ye, Y. Lin, X. Yao, J. Thorne, E. Liu, G. McMahon, J. Zhu, A. Javey, J. Guo, D. Wang, Enabling unassisted solar water splitting by iron oxide and silicon, Nat. Commun. 6 (2015) 7447-7452.

[28] L. Bian, H. Li, Y. Li, J. Nie, F. Dong, H. Dong, et al., Enhanced Photovoltage Response of Hematite-X-Ferrite Interfaces (X= Cr, Mn, Co, or Ni), Nanoscale Res. Lett. 12 (2017) 136-141.

[29] S. Shen, Toward efficient solar water splitting over hematite photoelectrodes, J. Mater. Res. (2013) 1–18.

[30] M.J. Katz, S.C. Riha, N.C. Jeong, A.B.F. Martinson, O.K. Farha, J.T. Hupp, Toward solar fuels: Water splitting with sunlight and “rust”?, Coord. Chem. Rev. 256 (2012) 2521–2529.

[31] K. Ulman, M. Nguyen, N. Seriani, R. Gebauer, K. Ulman, M. Nguyen, et al.,

ACCEPTED MANUSCRIPT

Passivation of surface states of α-Fe_2O_3 (0001) surface by deposition of Ga_2O_3 overlayers : A density functional theory study, J. Chem. Phys. 144 (2016) 94701–94706.

[32] S. Hussain, S. Hussain, A. Waleed, M.M. Tavakoli, Z. Wang, S. Yang, et al., Fabrication of $CuFe_2O_4$/α-Fe_2O_3 Composite Thin Films on FTO Coated Glass and 3-D Nanospike Structures for Efficient Photoelectrochemical Water Splitting, ACS Appl. Mater. Interfaces. 8 (2016) 35315–35322.

[33] H. Li, D. Niu, D. Liu, W. Huang, X. Zhang, Understanding the enhanced photoelectrochemical activity of Ta doped hematite, J. Mol. Struct. 1139 (2017) 104–110.

[34] T. Hisatomi, F. Le Formal, M. Cornuz, J. Brillet, N. Tétreault, K. Sivula, et al., Cathodic shift in onset potential of solar oxygen evolution on hematite by 13-group oxide overlayers, Energy Environ. Sci. 4 (2011) 2512–2515.

[35] F. Le Formal, N. Tétreault, M. Cornuz, T. Moehl, M. Grätzel, K. Sivula, Passivating surface states on water splitting hematite photoanodes with alumina overlayers, Chem. Sci. (2011) 737–743.

[36] M.G. Ahmed, I.E. Kretschmer, T.A. Kandiel, A.Y. Ahmed, F.A. Rashwan, D.W. Bahnemann, et al., A Facile Surface Passivation of Hematite Photoanodes with TiO_2 Overlayers for Efficient Solar Water Splitting, Appl. Mater. Interfaces. 7 (2015) 24053–24062.

[37] X. Yang, R. Liu, C. Du, P. Dai, Z. Zheng, D. Wang, Improving Hematite-based Photoelectrochemical Water Splitting with Ultrathin TiO_2 by Atomic Layer Deposition, Appl. Mater. Interfaces. 6 (2014) 12005–12011.

[38] B. Klahr, S. Gimenez, F. Fabregat-Santiago, T. Hamann, J. Bisquert, Water oxidation at hematite photoelectrodes: The role of surface states, J. Am. Chem. Soc. 134 (2012) 4294–4302.

[39] M. Barroso, A.J. Cowan, S.R. Pendlebury, M. Grätzel, D.R. Klug, J.R. Durrant, The role of cobalt phosphate in enhancing the photocatalytic activity of α-Fe_2O_3 toward water oxidation., J. Am. Chem. Soc. 133 (2011) 14868–14871.

[40] J. Brillet, M. Cornuz, F. Le Formal, J.-H. Yum, M. Grätzel, K. Sivula, Examining architectures of photoanode–photovoltaic tandem cells for solar water splitting, J. Mater. Res. 25 (2010) 17–24.

[41] L. Steier, I. Herraiz-cardona, S. Gimenez, F. Fabregat-Santiago, J. Bisquert, S.D. Tilley, et al., Understanding the Role of Underlayers and Overlayers in Thin Film Hematite Photoanodes, Mater. Views. 24 (2014) 7681–7688.

[42] S. Shen, M. Li, L. Guo, J. Jiang, S.S. Mao, Surface passivation of undoped hematite nanorod arrays via aqueous solution growth for improved photoelectrochemical water splitting, J. Colloid Interface Sci. 427 (2014) 20–24.

[43] M. Zhang, W. Luo, N. Zhang, Z. Li, T. Yu, Z. Zou, A facile strategy to passivate surface states on the undoped hematite photoanode for water splitting, Electrochem. Commun. 23 (2012) 41–43.

[44] A. Cots, D. Cibrev, P. Bonete, R. Gómez, Hematite Nanorod Electrodes Modified with Molybdenum: Photoelectrochemical Studies, ChemElectroChem. 4 (2016) 585–593.

[45] Y. Uwamino, T. Ishizuka, H. Yamatera, X-ray photoelectron spectroscopy of rare-earth compounds, J. Electron Spectros. Relat. Phenomena. 34 (1984) 67–78.

ACCEPTED MANUSCRIPT

[46] N. Hamnabard, Y. Hanifehpour, B. Khomami, S. Woo, Synthesis , characterization and photocatalytic performance of Yb-doped CdTe nanoparticles,Mater. Lett. 145 (2015) 253–257.

[47] M. Anwar, C.A. Hogarth, R. Bulpett, Effect of substrate temperature and film thickness on the surface structure of some thin amorphous films of MoO_3 studied by X-ray photoelectron spectroscopy (ESCA), J. Mater. Sci. 24 (1989) 3087–3090.

[48] A. Kleiman-Shwarsctein, Y.-S. Hu, A.J. Forman, G.D. Stucky, E.W. McFarland, Electrodeposition of α-Fe_2O_3 Doped with Mo or Cr as Photoanodes for Photocatalytic Water Splitting, J. Phys. Chem. C. 112 (2008) 15900–15907.

[49] B.V.R. Chowdari, K.L. Tan, W.T. Chia, R. Gopalakrishnan, X-ray photoelectron spectroscopic studies of molybdenum phosphate glassy system, J. Non. Cryst. Solids. 119 (1990) 95–102.

[50] S. Chatman, C.I. Pearce, K.M. Rosso, Charge Transport at Ti-Doped Hematite (001)/Aqueous Interfaces, Chem. Mater. 27 (2015) 1665–1673.

[51] H. Dotan, K. Sivula, M. Grätzel, A. Rothschild, S.C. Warren, Probing the photoelectrochemical properties of hematite (α-Fe_2O_3) electrodes using hydrogen peroxide as a hole scanvenger, Energy Environ. Sci. 4 (2011) 958-964.

[52] S. Park, H. Jin, C. Woo, H. Jo, S. Sik, S. Won, et al., Sn self-doped α-Fe_2O_3 nanobranch arrays supported on a transparent, conductive SnO_2 trunk to improve photoelectrochemical water oxidation, Int. J. Hydrogen Energy. 39 (2014) 16459-16467.

[53] C.X. Kronawitter, J.R. Bakke, D.A. Wheeler, W.C. Wang, C. Chang, B.R. Antoun, et al., Electron Enrichment in 3d Transition Metal Oxide Hetero-Nanostructures, Nano Lett. 11 (2011) 3855–3861.

[54] M. Tallarida, C. Das, D. Cibrev, K. Kukli, A. Tamm, M. Ritala, et al., Modification of Hematite Electronic Properties with Trimethyl Aluminum to Enhance the Efficiency of Photoelectrodes, J. Phys. Chem. Lett. 5 (2014) 3582–3587.

ACCEPTED MANUSCRIPT

Figure captions:

Figure 1. Top-view (A and B) and cross-sectional (C and D) FE-SEM images of pristine hematite (A and C) and hematite modified with the addition of 4.8 nmol Yb·cm^{-2} (H_Yb2) (B and D).

Figure 2. (a) 2p Fe, (b) 4d Yb and (c) 3d Mo XPS spectra for different hematite electrodes.

Figure 3. Voltammetric curves measured in aqueous N_2-purged 1M NaOH, obtained in the dark for pristine hematite (black) and hematite modified with 4.8 nmol Yb·cm^{-2} (H_Yb2) (red).

Figure 4. Linear voltammograms obtained in aqueous N_2-purged 1M NaOH under illumination (250 mW·cm^{-2}, λ>350nm) for pristine hematite (black) and hematite modified with different nmol of Yb·cm^{-2}. The inset shows the photocurrent obtained at 0.23 V as a function of the Yb loading.

Figure 5. Linear voltammograms obtained in aqueous N_2-purged 1M NaOH under illumination (250 mW·cm^{-2}, λ>350nm) for pristine hematite (black) and hematite modified with 4.8 nmol Yb·cm^{-2} (H_Yb2) (red): under (a) EE and (b) SE illumination. The inset in panel a shows photocurrent transients under EE illumination for pristine hematite (black) and hematite modified with 4.8 nmol Yb·cm^{-2} (H_Yb2) (red) at 0.23 V vs. Ag/AgCl.

Figure 6. Current density vs potential measured in N_2-purged aqueous 1M NaOH. (a) Cyclic voltammograms obtained in the dark, (b) linear voltammograms obtained under EE illumination (250 mW·cm^{-2}, λ>350nm) and (c) linear voltammograms obtained under SE illumination (250 mW·cm^{-2}, λ>350nm) for pristine hematite (black), hematite modified with 4.8 nmol Yb·cm^{-2} (H_Yb2) (red), hematite modified with 6.8 nmol Mo·cm^{-2} (H_Mo)(green) and hematite modified with 4.8 nmol Yb·cm^{-2} first and then 6.8 nmol Mo·cm^{-2} (H_Yb2_Mo) (blue) and with 6.8 nmol Mo·cm^{-2} first and then with 4.8 nmol Yb·cm^{-2} (H_Mo_Yb2) (purple).

Figure 7. Mott-Schottky plots for α-Fe_2O_3 electrodes, both pristine and modified with 4.8 nmol Yb·cm^{-2} (H_Yb2). Data obtained in the dark with a frequency of 1kHz in N_2-purged 1M NaOH.

Figure 8. Nyquist plots for pristine hematite (black), hematite modified with 4.8 nmol Yb·cm^{-2} (H_Yb2) (red) and hematite modified with 6.8 nmol Mo·cm^{-2} first and then with 4.8 nmol Yb·cm^{-2} (H_Mo_Yb2) (purple) (a) at -0.30 V vs. Ag/AgCl and (b) at 0.23 V vs. Ag/AgCl under illumination (250 mW·cm^{-2}, λ>350nm) in N_2-purged aqueous 1M NaOH.

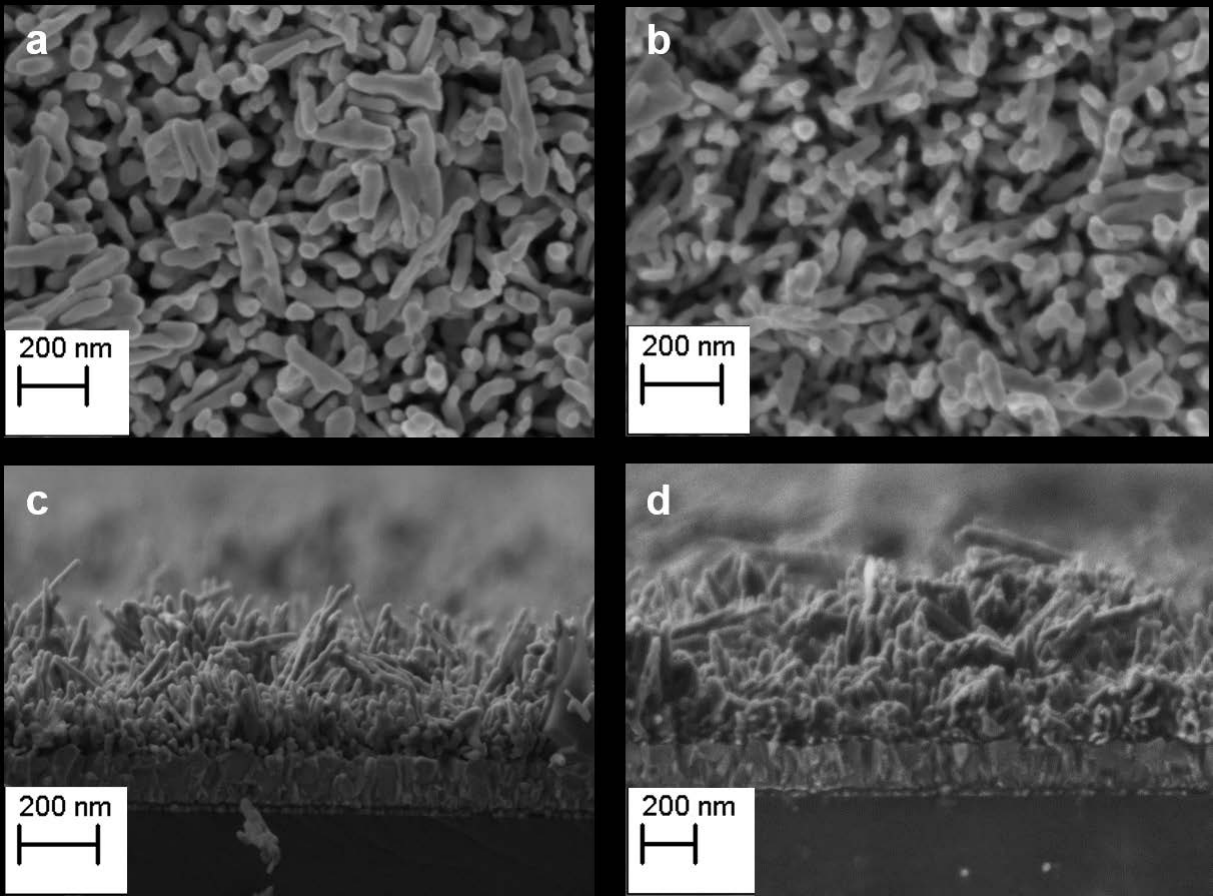
a
200 nm
b
200 nm
c
200 nm
d
200 nm

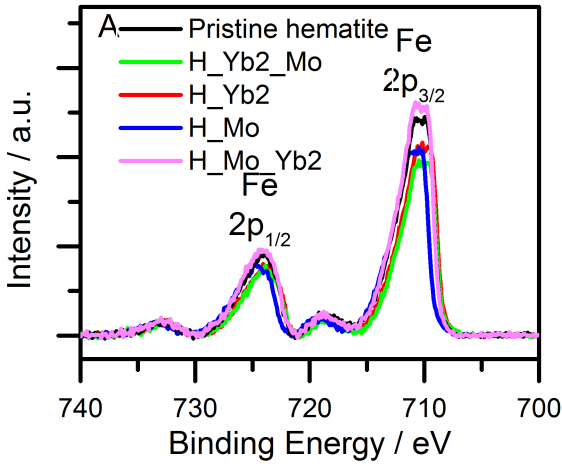
A
Pristine hematite
H_Yb2_Mo
H_Yb2
H_Mo
H_Mo_Yb2
Fe
2p3/2
Fe
2p1/2
Intensity / a.u.
740
730
720
710
700
Binding Energy / eV

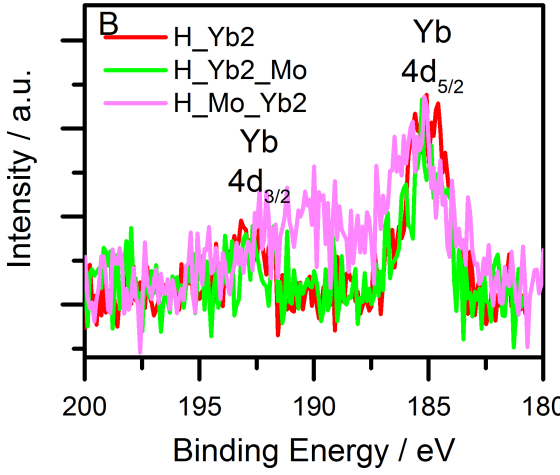
B
H_Yb2
H_Yb2_Mo
H_Mo_Yb2
Yb
4d5/2
Yb
4d3/2
Intensity / a.u.
200
195
190
185
180
Binding Energy / eV

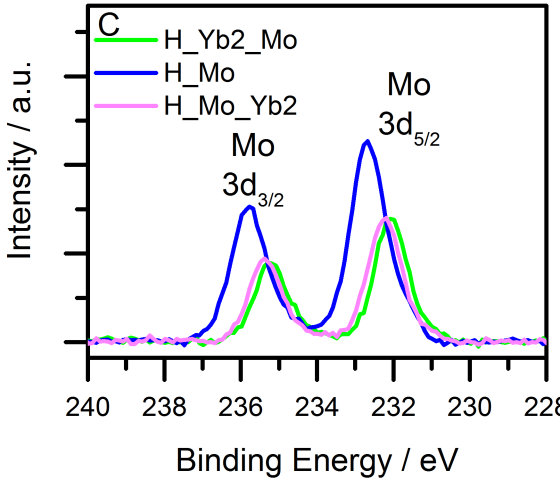
C
H_Yb2_Mo
H_Mo
H_Mo_Yb2
Mo
3d5/2
Mo
3d3/2
Intensity / a.u.
240
238
236
234
232
230
228
Binding Energy / eV

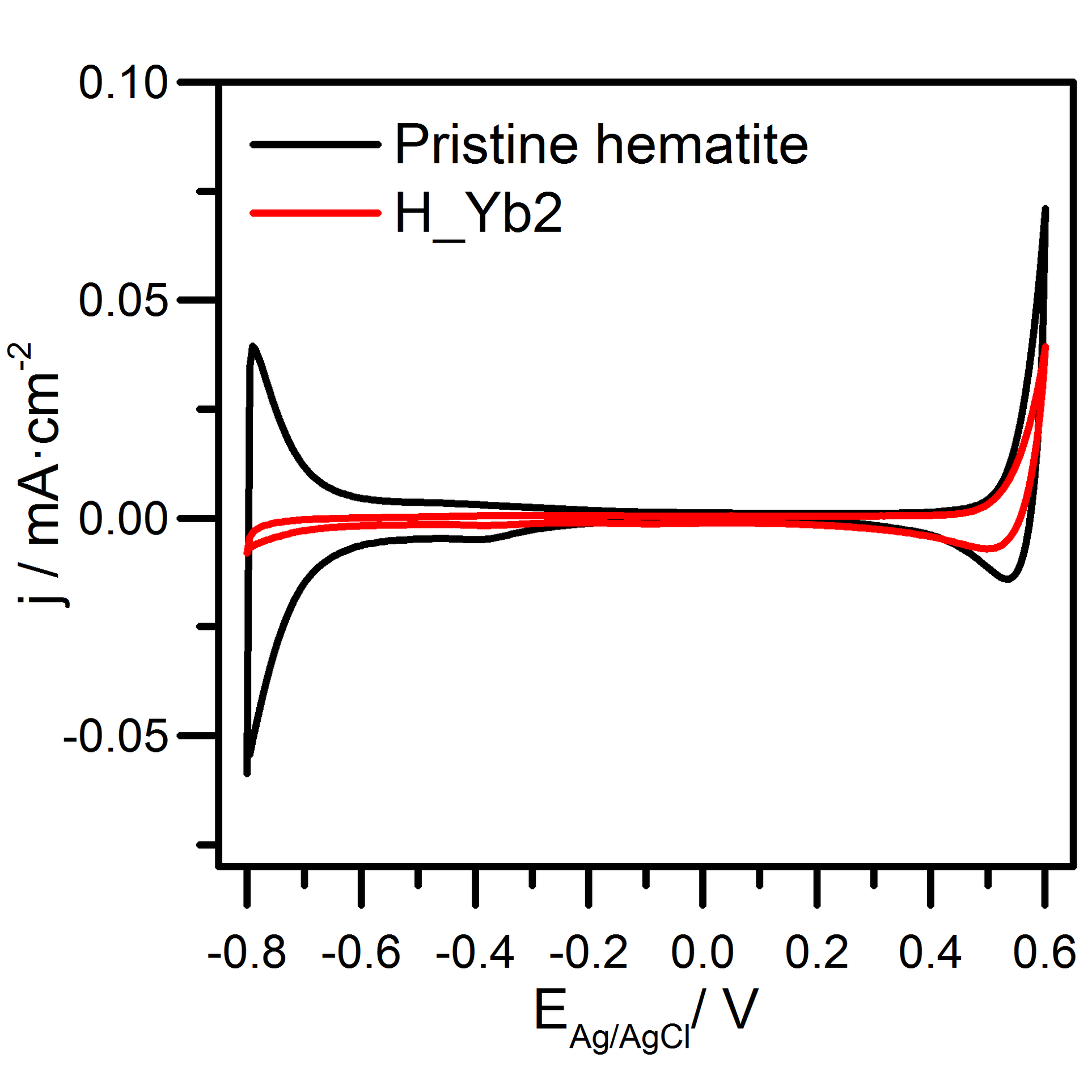
Pristine hematite
H_Yb2
0.10
0.05
0.00
-0.05
j / mA·cm-2
-0.8
-0.6
-0.4
-0.2
0.0
0.2
0.4
0.6
E Ag/AgCl / V

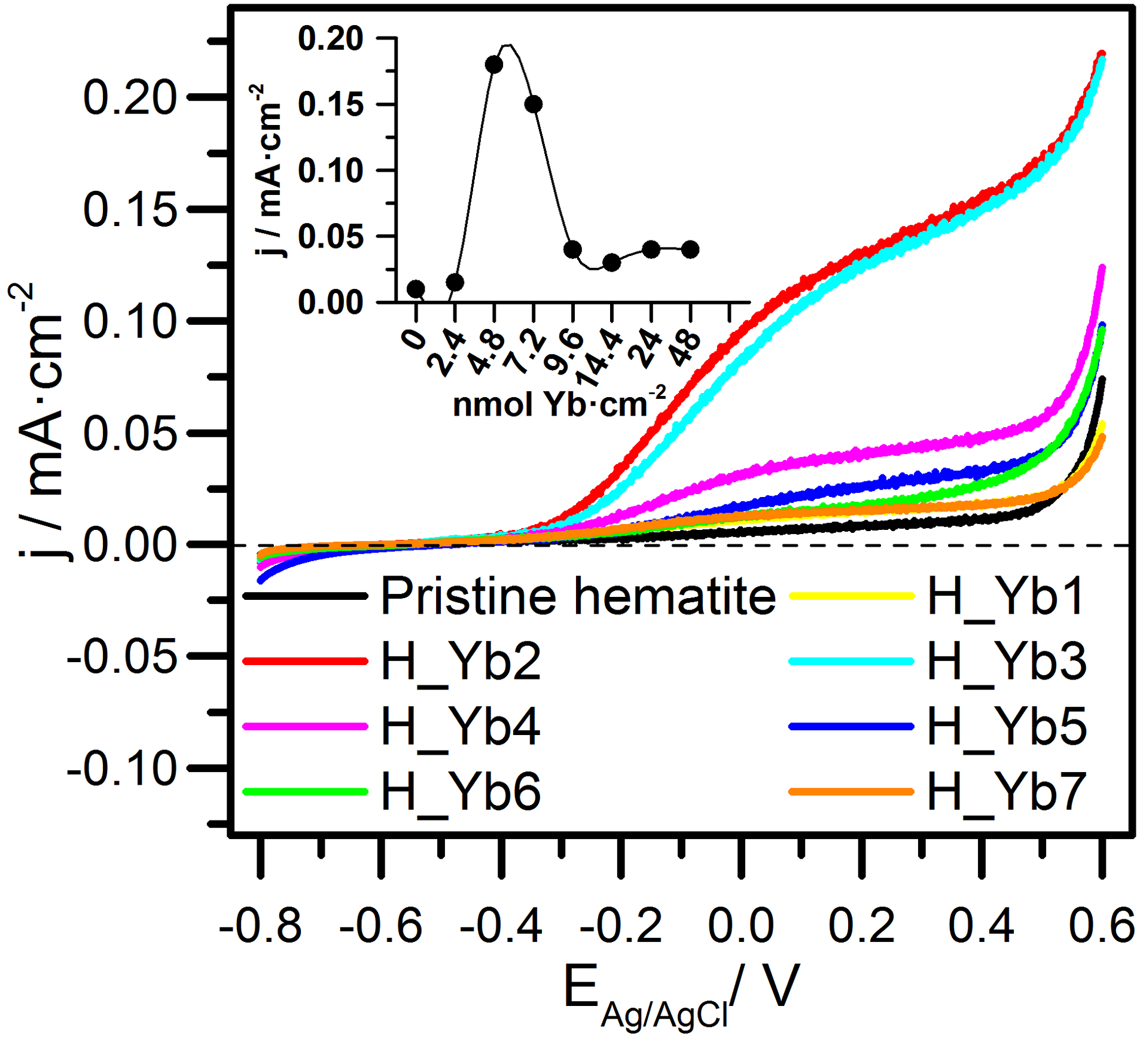
0.20
0.15
0.10
0.05
0.00
-0.05
-0.10
j / mA·cm-2
-0.8
-0.6
-0.4
-0.2
0.0
0.2
0.4
0.6
E Ag/AgCl / V
Pristine hematite
H_Yb1
H_Yb2
H_Yb3
H_Yb4
H_Yb5
H_Yb6
H_Yb7
0.20
0.15
0.10
0.05
0.00
j / mA·cm-2
0
2.4
4.8
7.2
9.6
14.4
24
48
nmol Yb·cm-2

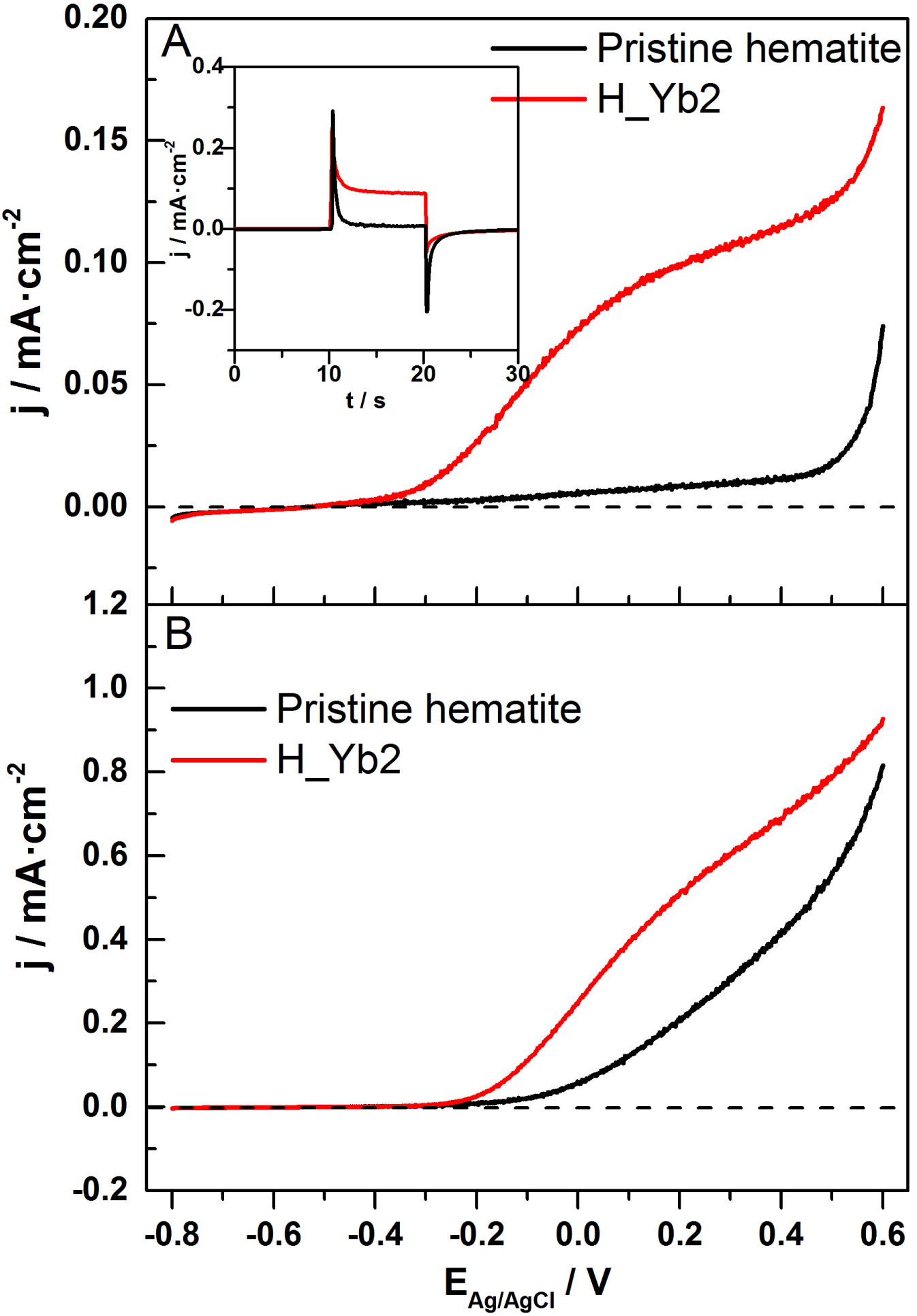
A
Pristine hematite
H_Yb2
j / mA·cm-2
t / s
B
Pristine hematite
H_Yb2
j / mA·cm-2
E Ag/AgCl / V

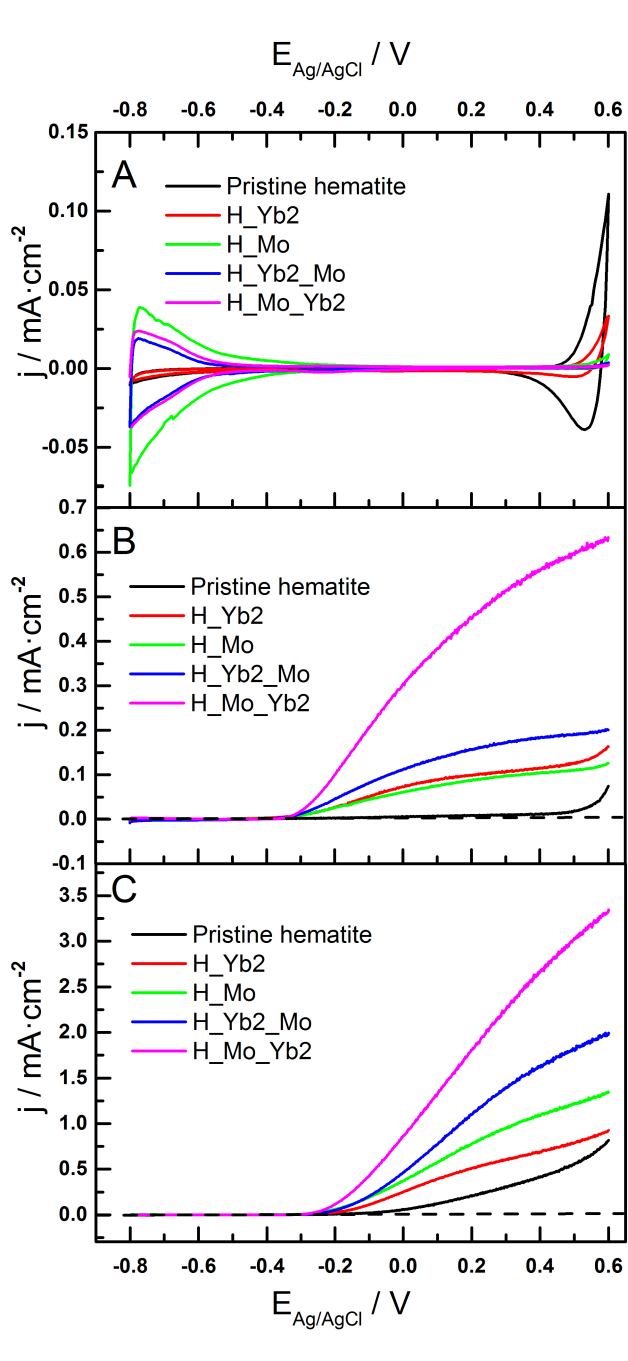
E Ag/AgCl / V
-0.8 -0.6 -0.4 -0.2 0.0 0.2 0.4 0.6
A
Pristine hematite
H_Yb2
H_Mo
H_Yb2_Mo
H_Mo_Yb2
j / mA·cm-2
0.15 0.10 0.05 0.00 -0.05 -0.7
B
Pristine hematite
H_Yb2
H_Mo
H_Yb2_Mo
H_Mo_Yb2
j / mA·cm-2
0.6 0.5 0.4 0.3 0.2 0.1 0.0 -0.1
C
Pristine hematite
H_Yb2
H_Mo
H_Yb2_Mo
H_Mo_Yb2
j / mA·cm-2
3.5 3.0 2.5 2.0 1.5 1.0 0.5 0.0
-0.8 -0.6 -0.4 -0.2 0.0 0.2 0.4 0.6
E Ag/AgCl / V

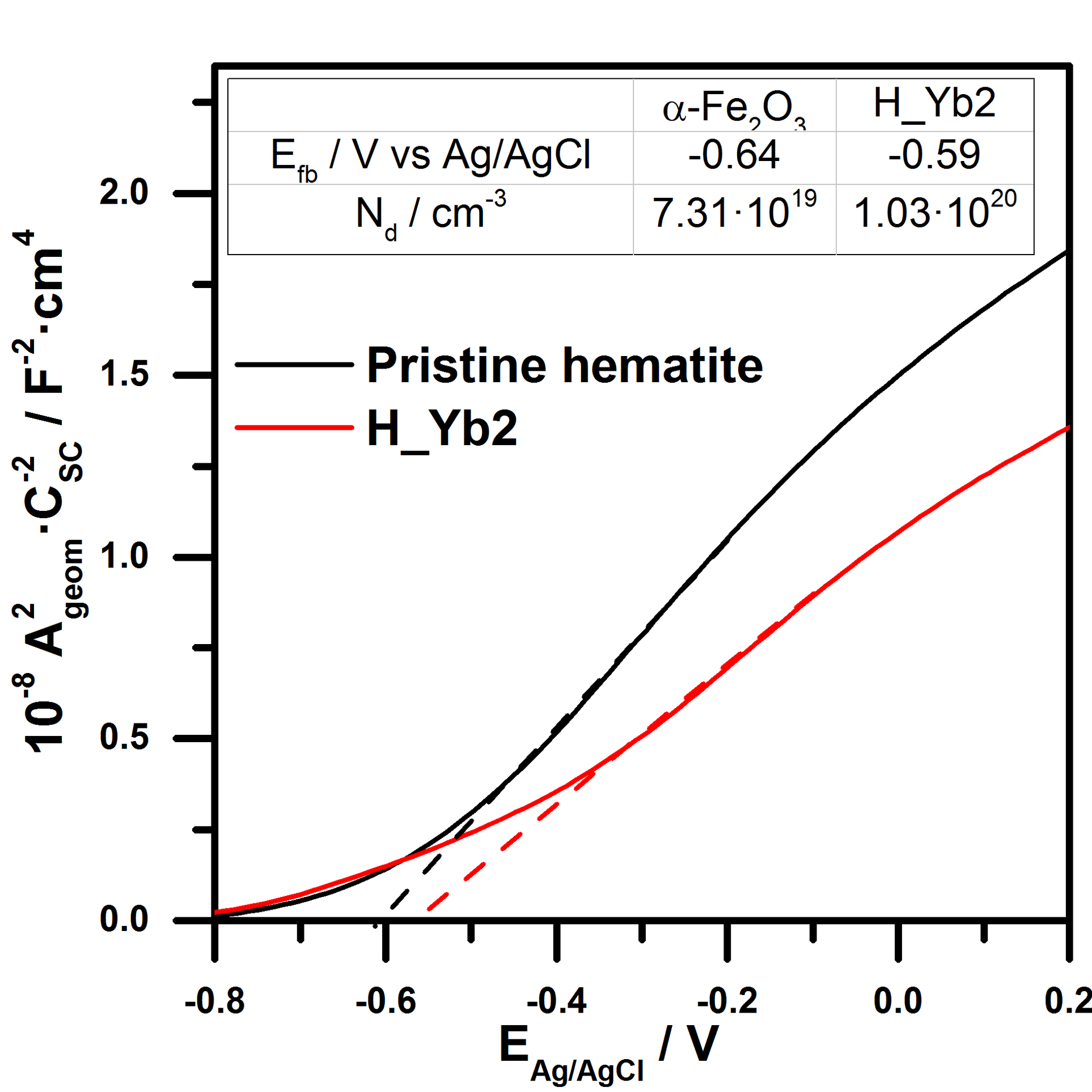
α-Fe2O3
H_Yb2
Efb / V vs Ag/AgCl
-0.64
-0.59
Nd / cm-3
7.31·10^19
1.03·10^20
Pristine hematite
H_Yb2
10-8 A2geom·C-2sc / F-2·cm4
2.0
1.5
1.0
0.5
0.0
-0.8
-0.6
-0.4
-0.2
0.0
0.2
EAg/AgCl / V

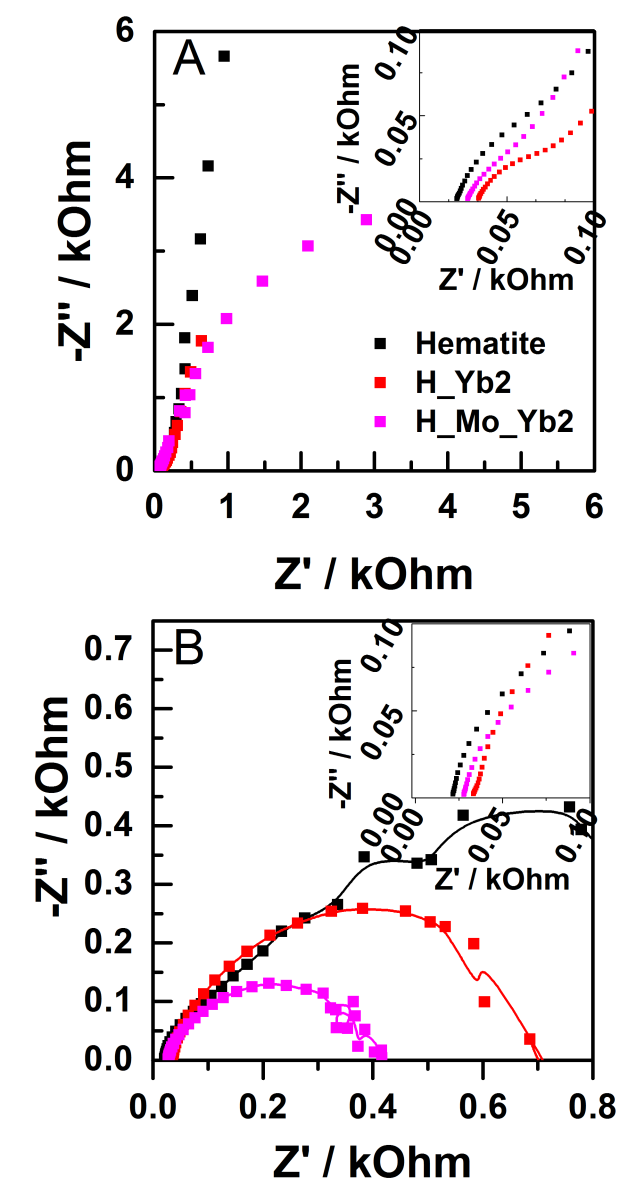
A
-Z'' / kOhm
Z' / kOhm
Hematite
H_Yb2
H_Mo_Yb2
B
-Z'' / kOhm
Z' / kOhm

ACCEPTED MANUSCRIPT

Table 1. Molar concentrations and quantity of moles added per cm^2 of the ytterbium precursor and the nomenclature employed. The letter H corresponds to hematite.

Nomenclature employed	**[$YbCl_3 \cdot 6H_2O$] / mM**	**Yb / nmol·cm^{-2}**
H	0	0
H_Yb1	0.072	2.4
H_Yb2	0.144	4.8
H_Yb3	0.216	7.2
H_Yb4	0.288	9.6
H_Yb5	0.432	14.4
H_Yb6	0.720	24
H_Yb7	1.440	48